Multisensor Characterization of Mammatus

SILKE TRÖMEL,[a] ALEXANDER V. RYZHKOV,[b] MALTE DIEDERICH,[a] KAI MÜHLBAUER,[a]
STEFAN KNEIFEL,[c] JEFFREY SNYDER,[b] AND CLEMENS SIMMER[a]

[a] *Meteorological Institute, University of Bonn, Bonn, Germany*
[b] *Cooperative Institute for Mesoscale Meteorological Studies, University of Oklahoma, and NOAA/OAR/ National Severe Storms Laboratory, Norman, Oklahoma*
[c] *Institute for Geophysics and Meteorology, University of Cologne, Cologne, Germany*

(Manuscript received 14 May 2016, in final form 28 August 2016)

ABSTRACT

Multisensor observations of anvil mammatus are analyzed in order to gain a more detailed understanding of their spatiotemporal structure and microphysical characterization. Remarkable polarimetric radar signatures are detected for the Pentecost 2014 supercell in Northrhine Westfalia, Germany, and severe storms in Oklahoma along their mammatus-bearing anvil bases. Radar reflectivity at horizontal polarization Z_H and cross-correlation coefficient ρ_{HV} decrease downward toward the bottom of the anvil while differential reflectivity Z_{DR} rapidly increases, consistent with the signature of crystal depositional growth. The differential reflectivity Z_{DR} within mammatus exceeds 2 dB in the Pentecost storm and in several Oklahoma severe convective storms examined for this paper. Observations from a zenith-pointing Ka-band cloud radar and a Doppler wind lidar during the Pentecost storm indicate the presence of a supercooled liquid layer of at least 200–300-m depth near the anvil base at temperatures between $-15°$ and $-30°$C. These liquid drops, which are presumably generated in localized areas of vertical velocities of up to 1.5 m s^{-1}, coexist with ice particles identified by cloud radar. The authors hypothesize that pristine crystals grow rapidly within these layers of supercooled water, and that oriented planar ice crystals falling from the liquid layers lead to high Z_{DR} at precipitation radar frequencies. A mammatus detection strategy using precipitation radar observations is presented, based on a methodology so far mainly used for the detection of updrafts in convective storms. Owing to the presence of a supercooled liquid layer detected above the mammatus lobes, the new detection strategy might also be relevant for aviation safety.

1. Introduction

Mammatus—which is the more common term for the internationally accepted terminology mamma (World Meteorological Organization 1975, 1987)—appear as a cellular pattern of lobes, bulges, or protuberances "hanging" underneath the cloud base (Glickman 2000; Schultz et al. 2006). Mammatus at the underside of cumulonimbus anvils is the most commonly recognized, but mammatus also form in cirrus, cirrocumulus, altocumulus, altostratus, stratocumulus, and volcanic ash clouds (e.g., Stith 1995; Kollias et al. 2005; Schultz et al. 2006). Schultz and Hancock (2016) argue that lobes associated with contrails cannot be classified as mammatus. While mammatus frequently attract photographers, their essential atmospheric conditions, formation mechanisms, dynamics, and macro- and microphysical properties are still not completely understood; Schultz et al. (2006) provide a critical review of 10 formation mechanisms that have been suggested during the last decades. Reported observations are mostly restricted to only one measurement device, like ground-based Doppler radar (Martner 1995, 1996), airborne Doppler radar (Winstead et al. 2001), ground-based Doppler cloud radar (Kollias et al. 2005), lidar (Wang and Sassen 2006; Platt et al. 2002), aircraft penetrations, or photographs. Thus, information about the larger-scale spatial distribution of mammatus and their evolution is scarce at best.

Available mammatus observations differ with respect to the type of particles within the lobes. Hlad (1944) reports on an aircraft flight through mammatus and characterizes them as rain sacks and speculates that

Denotes Open Access content.

Corresponding author address: Dr. Silke Trömel, Auf dem Hügel 20, 53121 Bonn, Germany.
E-mail: silke.troemel@uni-bonn.de

DOI: 10.1175/MWR-D-16-0187.1

strong upward motion must prevent the raindrops from falling out. Observations and considerations by Clough and Franks (1991) and Stith (1995) suggest ice particles as the predominant constituents of mammatus. Temperatures were far below 0°C level in most observations, thus ice particles are likely dominating mammatus. Liquid layers near the top of many cold cloud systems (stratiform and convective clouds) have been observed by aircraft measurements of Hobbs and Rangno (1985) and Rauber and Grant (1986) even at temperatures below −30°C. Rauber and Tokay (1991) conclude from simulations that in localized updrafts "the imbalance between the condensate supply rate and the bulk ice crystal mass growth at a wide range of temperatures and updraft speeds is sufficient to produce this liquid layer (p. 1005)," because the ice crystals concentration might be too small to deplete the generated liquid water. Thus, if updrafts exist in mammatus, then a mixture of ice and liquid particles is possible even high above the 0°C level.

In this paper, we characterize the microphysics of cumulonimbus anvil mammatus observed on the upshear and downshear sides of the outflow anvil of an intense supercell on 9 June 2014 (Pentecost) in Northrhine Westfalia, Germany, based on multisensor measurements. We exploit the polarimetric information compiled in the 3D mosaic of differential reflectivity Z_{DR}, radar reflectivity at horizontal polarization Z_H, cross-correlation coefficient $\rho_{HV,}$ and specific differential phase K_{DP} for an automated detection and characterization of the spatiotemporal distribution of mammatus including composition and inherent circulation.

According to the three supercell archetypes (Moller et al. 1990, 1994; Beatty et al. 2008)—"classic," "low precipitation" (LP), and "high precipitation" (HP)—the Pentecost event was an HP supercell. The evolution of the event is captured by a Germany-wide 3D composite based on the polarimetric C-band radar network of the German Weather Service [Deutscher Wetterdienst (DWD)]; the composite has 1-km horizontal and 250-m vertical grid spacing and is provided in 5-min intervals. These observations are complemented with time series of vertical profiles from a suite of remote sensing measurements from the Jülich Observatory for Cloud Evolution (JOYCE) (Löhnert et al. 2015) located at the research center Jülich, Germany. The JOYCE observations from a 35.5-GHz cloud radar, a 1.5-μm Doppler lidar, and a total sky imager provide valuable information during the passage of the supercell and the mammatus bearing anvil over Jülich. The supercell also grazed the Meteorological Institute of the University of Bonn, Bonn, Germany, located about 50 km to the east of JOYCE, where a polarimetric X-band radar provides—besides ordinary volume scans—vertical cross sections [so-called range–height indicator (RHI) scans] with small grid intervals (75 m) and birdbath scans (vertical observations with a turning antenna dish) every 5 min. A collocated ceilometer monitored the cloud-base height and provided additional insight into the outer structure of the mammatus lobes. The findings from the Pentecost storm are complemented by polarimetric radar observations of mammatus associated with supercells in Oklahoma.

Section 2 provides a synoptic characterization of the Pentecost event, while section 3 describes in detail the multisensor database available for the analysis. In section 4, we introduce our method for mammatus detection, and section 5 contains the interpretation and discussion of the multisensor measurements obtained during the Pentecost event. Section 6 presents supporting mammatus observations from Oklahoma, and section 7 derives a general characterization of anvil mammatus. Section 8 provides a summary and conclusions.

2. The Pentecost storm on 9 June 2014 in Northrhine Westfalia, Germany

During the 2014 Pentecost weekend, a series of severe supercell storms occurred in northern France, Belgium, Luxembourg, the Netherlands, and, especially, Germany, following a heatwave in early June in combination with a Spanish plume synoptic weather pattern. The Spanish plume (e.g., van Delden 1998; Lewis and Gray 2010) refers to a weather pattern in which moist air capped by warmer but dry air moves into northwestern Europe from the southwest. This pattern can create heatwaves and support the buildup of substantial convective available potential energy that can be released when, for example, air is lifted by low-level colder air approaching from the Atlantic, initiating intense convective storms. The radiosonde from Bergen (52.82°N, 9.93°E; about 380 km northeast of Jülich; the closest sounding available at this time) at 1800 UTC 9 June 2014 (Fig. 1) shows a rather moist boundary layer with little spread between temperature and dewpoint below a warm and dry well-mixed layer between 800 and 650 hPa that is characterized by a nearly dry adiabatic lapse rate. Steep midtropospheric lapse rates associated with this elevated mixed layer (EML) allows high convective available potential energy to develop. EMLs, which can keep storms isolated (e.g., Benjamin and Carlson 1986), are generated over the Iberian Plateau and advected by southwesterly flow—as was the case during the Pentecost event—over a warm, moist boundary layer, creating high potential energy and so-called "loaded gun" soundings. Such situations are responsible for the most severe weather events in Europe (Schaefer 1986). Low-level convergence (e.g., along a frontal boundary) can "push" boundary layer parcels through the layer of convective inhibition or the so-called

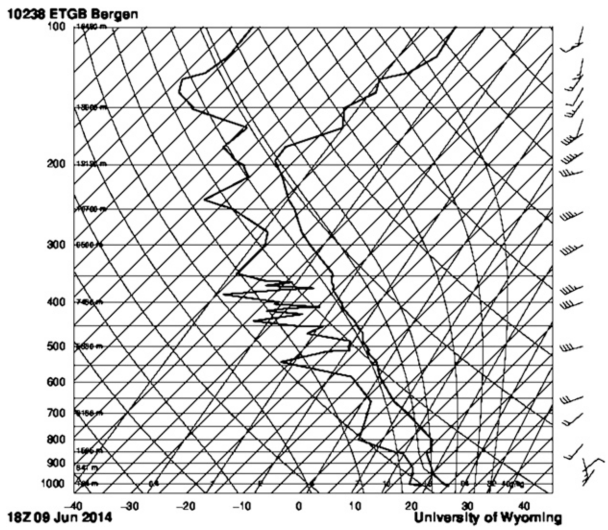

FIG. 1. Radiosounding at 1800 UTC 9 Jun 2014 measured in Bergen, Germany. (Source: University of Wyoming http://weather.uwyo.edu/upperair/sounding.html.)

cap sometimes found at the base of the EML and initiate convection; diabatic heating in the boundary layer can also remove convective inhibition and allow for the development of surface-based convection.

According to the Consortium for Small-Scale Modeling–European Union (COSMO-EU) analysis generated with the COSMO model [for details, see Doms and Schättler (2002) or Baldauf et al. (2011)], mean-layer convective available potential energy (ML-CAPE) reached 2000–2500 J kg^{-1} over large areas with peaks up to 3000 J kg^{-1} before and during this event. The atmosphere was further characterized by deep-layer bulk wind differences (wind difference between 0 and 6 km) of 15 m s^{-1} in central Germany. Radiosoundings, as well as the comparison of winds at 850 and 500 hPa in the COSMO-EU analysis, also revealed veering, resulting in 0–3-km storm-relative helicity of around 200 m^2 s^{-2}. Outbreaks of severe weather were reported on 9 and 10 June with the worst damage produced by one of the region's most violent storms in decades as it crossed the German state of North Rhine-Westphalia on 9 June. This particular storm caused six fatalities and produced devastating wind gusts up to 42 m s^{-1}, hail, and a flash flood in Düsseldorf, Germany. Besides the total sky imager (TSI) observations from JOYCE (see next section), photographs and YouTube videos from the public confirm long-lasting and widespread occurrence of mammatus during this event.

3. The multisensor database

Areal coverage of the storm and its evolution are provided by a Germany-wide 3D composite of polarimetric moments generated by the Hans-Ertel-Centre for Weather Research (HErZ; Simmer et al. 2016) with 1-km horizontal and 250-m vertical grid spacing. Each of the contributing radars monitors the evolution of precipitation in the 180-km vicinity with 1-km radial grid spacing; volume scans are collected at a 5-min interval and consist of 10 elevations ranging from 0.5° to 25°. A linear relation between path-integrated attenuation and differential phase shift is assumed in order to correct for attenuation-related biases of Z_H and Z_{DR}. Corrected scans are projected onto a 3D polar-stereographic grid, taking into account advection calculated from subsequent scans using cross correlation (Bellon et al. 1991; Anagnostou and Krajewski 1999).

The polarimetric X-band weather radar BoXPol, operated by the Transregional Collaborative Research Center TR32 (www.tr32.de; Simmer et al. 2015) and installed on a 30-m-tall building next to the Meteorological Institute of the University Bonn [50.73052°N, 7.071663°E, 99.9 m MSL, for details see Diederich et al. (2015)], provides continuous monitoring of precipitation in the 150-km range with 150-m radial grid spacing. BoXPol generates volume products every 5 min based on a volume scan with 10 elevation angles from 1° to 28°. In addition, a vertical scan (so-called birdbath scan) and a genuine RHI providing a vertical cross section at azimuth 225° (which, on average, is the direction where most precipitation events approach) complete the 5-min surveys. Collocated with BoXPol is a 1064-nm ceilometer/cloud height meter CHM15k [Jenoptik GmbH, Germany; Heese et al. (2010)] deployed at the Meteorological Institute of the University of Bonn; it provides the evolution of (uncalibrated) attenuated backscatter (β) profiles (Weitkamp 2005) and up to three cloud-base heights between 15 and 15 000 m in range.

JOYCE, located at the research center Jülich (50.9086°N, 6.4136°E, 111 m MSL), is equipped with a great variety of state-of-the-art remote sensing and in situ instruments intended to monitor the variability of the atmospheric water cycle and physical cloud properties. The Ka-band, polarimetric, Doppler cloud radar JOYRAD-35 [METEK GmbH, Germany; Görsdorf et al. (2015)], which operates at 35.5 GHz, provides vertical profiles of Doppler spectra and derived standard moments (reflectivity, mean Doppler velocity, Doppler spectral width, and linear depolarization ratio) between 150 m and 15 km above ground. The 1.5-μm streamline Doppler lidar [HALO Photonics, United Kingdom; Pearson et al. (2009)] provides wind speeds along the beam for arbitrary directions, from which vertical air motion and profiles of the horizontal wind speed and direction below cloud base are derived. The TSI (Long et al. 2006) records a hemispheric image every 20 s from which cloud cover and its partitioning in thin and opaque clouds is derived.

4. Radar-based detection of updrafts and mammatus

The observations and discussion contained in this paper are a rather unexpected result of an ongoing analysis of the German 3D polarimetric composite on the predictive power of updrafts indicated by Z_{DR} columns for intense rainfall over Germany. The methodology—described in more detail below—led to the areawide detection of mammatus during the Pentecost event and triggered the additional analyses including supportive observations presented here.

a. Differential reflectivity

Differential reflectivity Z_{DR}, expressed in units of dB, is the ratio of the linear radar reflectivity factors at horizontal and vertical polarizations Z_H and Z_V, respectively, where Z_{DR} is independent of hydrometeor number concentration but varies with hydrometeor shape, orientation, density, and refractive index. For an in-depth description of the information content of Z_{DR} in rain, we refer to Zrnić and Ryzhkov (1999), Bringi and Chandrasekar (2001), Doviak and Zrnić (2006), Chandrasekar et al. (2013), and Kumjian (2013). Owing to orientation effects (i.e., mean nonzero canting) Z_{DR} of ice particles can be either positive or negative (e.g., Oue et al. 2015). A further reduction in Z_{DR} is seen for frozen particles that are tumbling or those that have more random orientation (e.g., North et al. 2014; Pruppacher and Klett 1996). Both factors cause Z_{DR} of dry graupel and aggregated snowflakes to be much lower compared to rain; Z_{DR} of dry aggregated snow is usually between 0 and 0.2 dB due to the very low density of snow aggregates (Ryzhkov et al. 1998). High values may occur for well-oriented nonspherical ice particles (Oue et al. 2016). Accordingly, Z_{DR} is higher for single crystals like needles and plates compared to large aggregated dry snowflakes. The Z_{DR} of ice particles tends to be significantly lower than that of raindrops with a similar aspect ratio (i.e., the ratio of shortest to longest particle extension) due to the lower dielectric constant of ice (e.g., Zrnić and Ryzhkov 1999; Bringi and Chandrasekar 2001). Nevertheless, ice can be highly anisotropic and can have mean nonzero canting that result in higher or lower Z_{DR}.

b. Z_{DR} signals associated with mammatus

Enhanced Z_{DR} above the 0°C level, which sometimes appears as vertically extended columns (so-called Z_{DR} columns), is currently thought to be associated with supercooled liquid rain drops lofted by intense updrafts (e.g., Illingworth et al. 1987; Kumjian et al. 2014; Snyder et al. 2015). The Z_{DR} columns are considered as a potential future operational tool to quantify the extent and intensity of updrafts in convective storms and thus early signs of rainfall intensification and hail (Picca and Ryzhkov 2010; Kumjian et al. 2014; Weissmann et al. 2014; Snyder et al. 2015).

We generated a Z_{DR} column product following the method described in Picca and Ryzhkov (2010). The method is based on counting the number of vertical grid boxes above the environmental 0°C level with Z_{DR} exceeding a predetermined threshold of 1 or 2 dB; multiplication of the count with the grid box volume (1 km × 1 km × 0.25 km) results in a "Z_{DR} column volume" product. Increasing Z_{DR} column values in time indicate updraft intensification and, thus, potentially heavy precipitation and large hail.

Figure 2 shows a genuine RHI recorded by the polarimetric, X-band radar in Bonn (BoXPol), Germany, at 1830 UTC at 225° azimuth. Columns of enhanced Z_{DR} are visible (left panel in Fig. 2) in the precipitating part of the storm, which protrude above the 0°C level at around 3.8-km height at distances of about 28, 36, and 40–44 km from the radar. The typical wavy structures of mammatus can be seen in the sloping base of the leading (i.e., downshear) anvil. Mammatus may appear both in the leading and in the trailing anvil (e.g., Bluestein and Parks 1983). The horizontal width of individual mammatus lobes in the leading anvil of the supercell monitored by BoXPol (Fig. 2, right panel) is of the order of 1–3 km, while the vertical extents reach up to 1 km. This particular RHI was, however, just grazing the mammatus region and missed the most intense mammatus lobes. Reconstructed RHIs based on the BoXPol radar volume measurements across the center of the mammatus region, however, show indications of enhanced Z_{DR} values aloft (not shown).

The Z_{DR} column product for the C-band 3D radar composite (using Z_{DR} threshold of 1 dB) for the Pentecost event reveals surprising results at first glance; Fig. 3 shows on the right panel a snapshot of the detected Z_{DR} columns at 2020 UTC while the left panel displays near-surface Z_H with the typical bow echo (see section 2) clearly visible. A correlation analysis between these apparent Z_{DR} columns and near-surface Z_H for the Pentecost event reveals, however, that only most of these apparent Z_{DR} columns are short lived and do not produce meaningful precipitation. Additionally, many of the areas with positive Z_{DR} column depth actually emerged after the passage of the bow echo. The detected Z_{DR} signals at up to 50 km ahead of the areas of high near-surface Z_H do not appear to be the same as the "usual" Z_{DR} columns associated with strong convective storm updrafts; another mechanism seems to be behind the

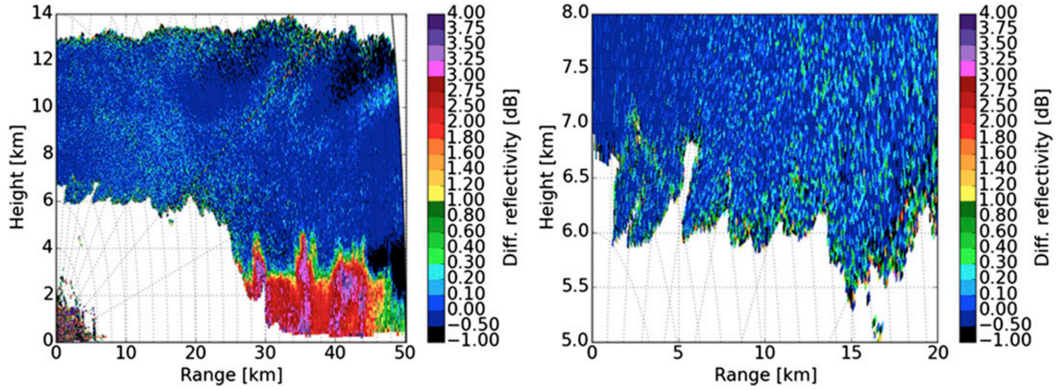

FIG. 2. Genuine range–height indicator (RHI) measured with the polarimetric X-band radar in Bonn (BoXPol), Germany, at 1830 UTC 9 Jun 2014 along azimuth 225°. (left) The polarimetric variable shown is differential reflectivity Z_{DR}. (right) A zoomed-in view of the mammatus region depicting Z_{DR} again. The 0°C level is around 4-km height.

enhanced Z_{DR} aloft that causes false alarms from the algorithm. In light of this, it appears that the algorithm is not only detecting Z_{DR} columns as they have commonly been observed and described (i.e., associated with deep updrafts in intense convective storms). As such, we will instead refer to these features (i.e., detections by the Z_{DR} column algorithm) as "Z_{DR} signals." The multisensor analysis detailed in section 5 will associate a large part of the Z_{DR} signals with anvil mammatus high above the 0°C level.

5. Synergistic observations of mammatus during the 2014 Pentecost event

The false alarms in the Z_{DR} column algorithm initiated a synergistic analysis of remote- sensing observations to explore the nature of the Z_{DR} signatures at the bases of the storm anvils. A snapshot for an area around JOYCE is shown in Fig. 4, which combines surface Z_H (color shading) with the pseudo-Z_{DR} column product (indicated by filled contour lines highlighting areas with 3, 6, or 8 vertically stacked grid boxes of $Z_{DR} > 1$ dB above the 0°C level) for each (x, y) coordinate at 1740 UTC. The straight blue line indicates the location of the vertical cross section displayed in Fig. 5. While the pseudo-Z_{DR} column product in Fig. 4 is based on interpolated composite data, the vertical cross section in Fig. 5 shows noninterpolated data, which let us connect the Z_{DR} signals at large distances from the primary storm cores to the high surface Z_H to the base of the anvil between 5 and 8 km.

The Z_{DR} values are found to increase toward the anvil bottom. The magnitudes at the underside of the anvil

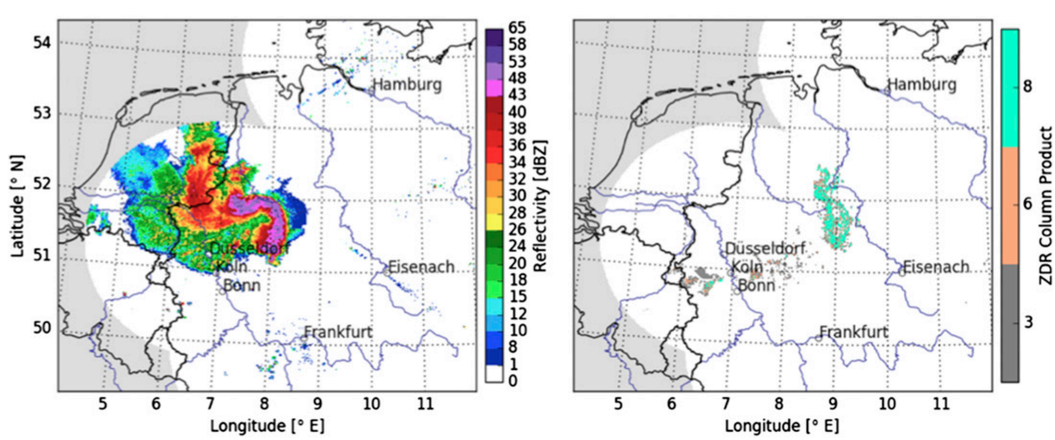

FIG. 3. Snapshot showing a zoomed-in view of the near-surface reflectivities Z_H observed at 2020 UTC 9 Jun 2014 in the northwestern part of Germany based on (left) the national 3D composite and (right) filled contour lines of the derived Z_{DR} column product indicating more than or equal to 3, 6, or 8 grid boxes with Z_{DR} greater than 1 dB in the vertical column above the 0°C level for each (x, y) coordinate.

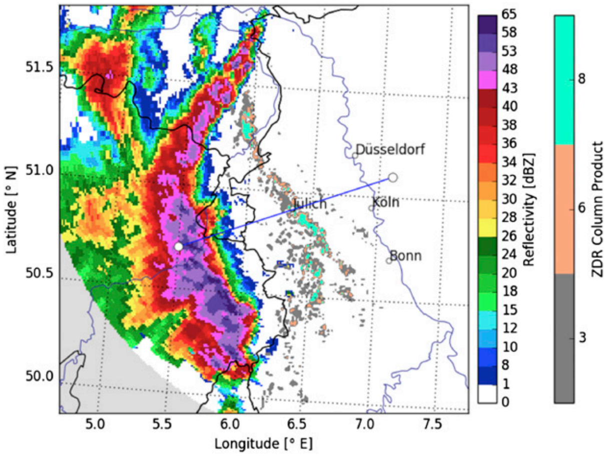

FIG. 4. A snapshot at 1740 UTC 9 Jun 2014 indicating surface reflectivity (color shading) and the Z_{DR} column product (filled contours) based on the national C-band radar composite for the area of Jülich and Bonn. The blue line indicates the position of the cross section shown in Fig. 5.

clearly exceeding 0.4 dB, which is the typical Z_{DR} we would expect from ordinary snow aggregates in anvils of deep convection (Homeyer and Kumjian 2015). Cross sections at the same location approximately 10 min before and after this time show maximal Z_{DR} values in the leading anvil region between 1.6 and 2.5 dB, and values between 1 and 1.4 dB are also observed in the trailing anvil. According to temperature-dependent ice particle habit growth (e.g., Bailey and Hallett 2009) and the temperatures at the anvil bottom (between −15° and −30°C), we expect preferential platelike crystal growth, and that by vapor deposition as suggested by synergistic measurements from JOYRAD-35 and the 1.5-μm Doppler lidar. These platelike crystals could explain the enhanced Z_{DR} we observe (cf. section 7c for a detailed discussion). The collocated vertical scans from the JOYCE cloud radar (JOYRAD-35) clearly hint at localized areas of upward motion and layers of supercooled liquid water in the mammatus region of the leading anvil of the storm, which indicates that the conditions for efficient depositional growth are favorable in these regions.

A zoomed-in view into the anvil underside of the most intense mammatus lobes, which passed the site around 1740 UTC, is shown in Fig. 6. The different panels show effective radar reflectivity factor Z_e, mean Doppler velocity, and Doppler spectral width. We utilize the backscattering profile of the 1.5-μm Doppler lidar

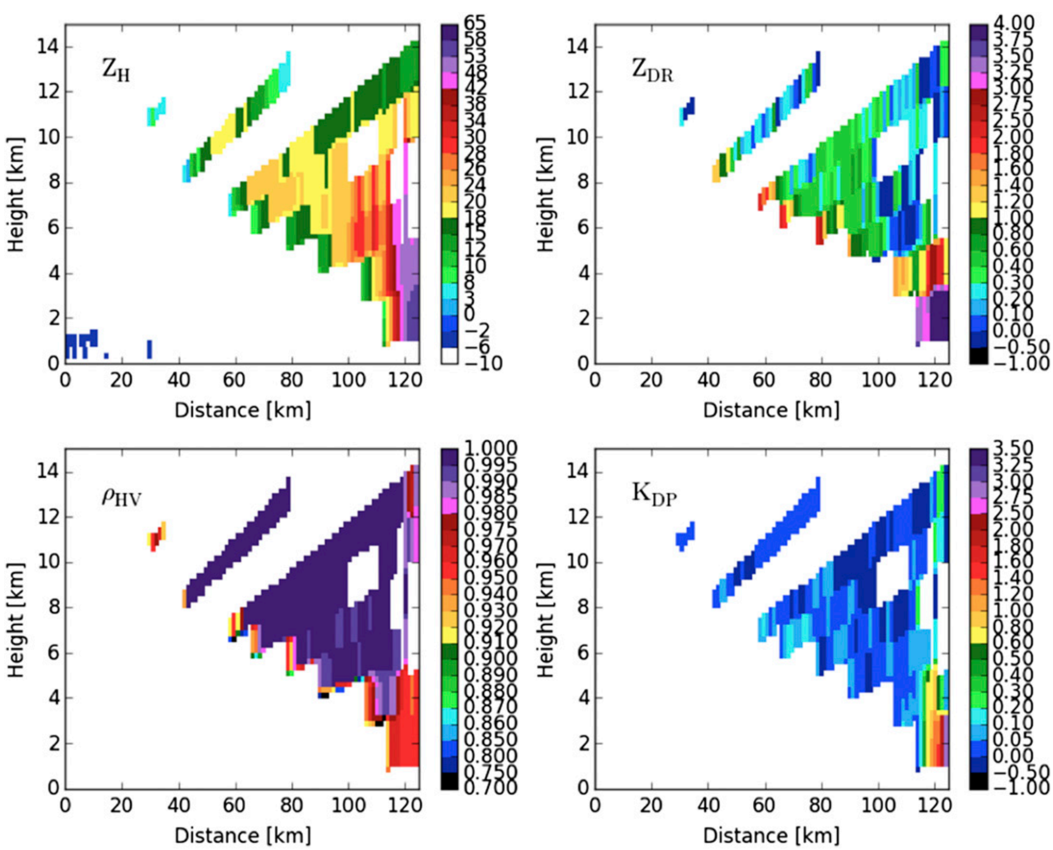

FIG. 5. Cross section through the 3D composite along the line indicated in Fig. 4 showing the polarimetric variables (top left) Z_H, (top right) Z_{DR}, (bottom left) ρ_{HV}, and (bottom right) K_{DP}.

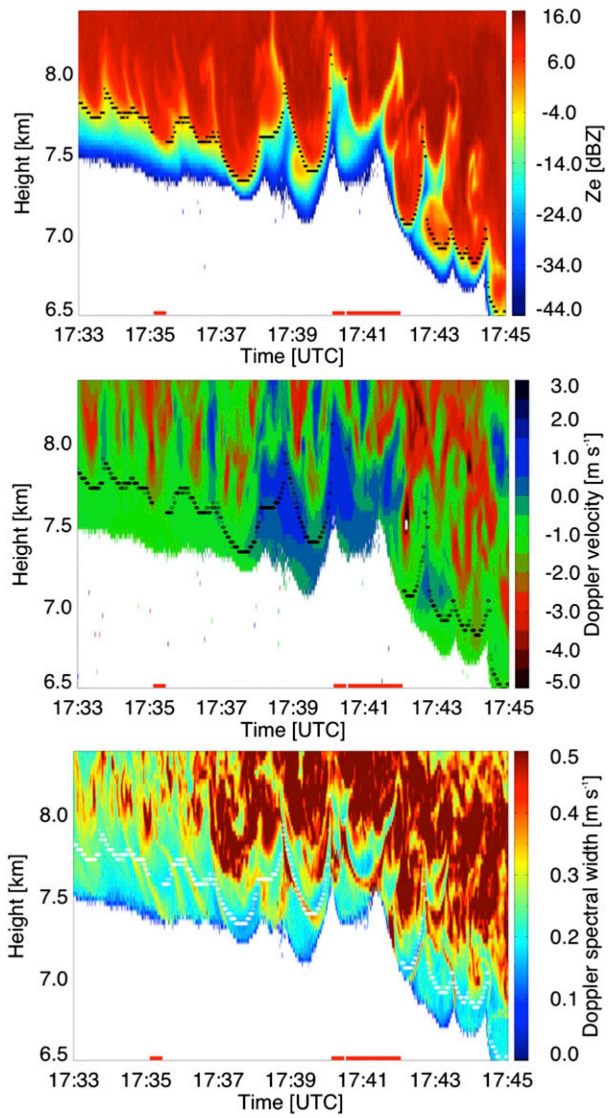

FIG. 6. Detailed zoomed-in view of the underside of the anvil with the most intense mammatus lobes. (top) Effective reflectivity factor, (middle) mean Doppler velocity (positive values show upward motion), and (bottom) spectral width measured at JOYCE between 1733 and 1745 UTC 9 Jun 2014 with the JOYRAD-35 Ka-band cloud radar. Overlaid black (top two panels) and white (bottom panel) dots represent the location of a liquid layer as identified with the collocated 1.5-μm Doppler lidar measurements (Fig. 7); the red line at the bottom of each panel indicates times where the Doppler lidar was not in vertically pointing mode.

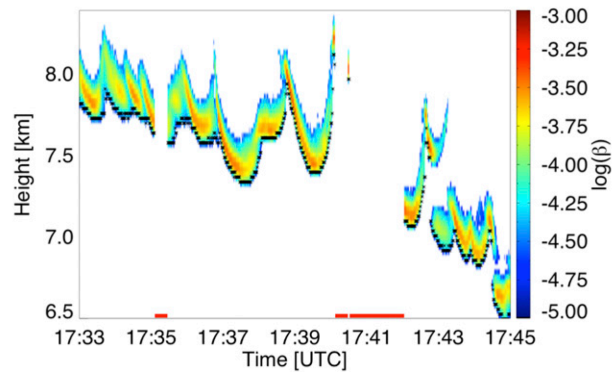

FIG. 7. As in Fig. 6, a detailed zoomed-in area of the underside of the anvil with the most intense mammatus lobes, but the logarithm of the attenuated backscattering coefficient measured by the 1.5-μm Doppler lidar is displayed. The red line at the bottom of the panel indicates times where the Doppler lidar was not in vertically pointing mode.

(Fig. 7) to detect the supercooled liquid water drops by applying a thresholding technique similar to Delanoë and Hogan (2010): a layer of supercooled liquid water causes a sudden increase in backscattering followed by a strong signal decrease due to attenuation by supercooled liquid water. The lidar signal is completely attenuated within approximately 200–300 m around the peak backscattering signal, which is a typical feature of liquid water [see also Hogan et al. (2004)] and suggests a minimum depth of the liquid layer of 200–300 m.

From the cloud radar and lidar observations alone, we cannot rule out frozen cloud droplets at high concentrations, which would appear very similar to liquid drops to a lidar. Collocated passive microwave observations, however, suggest liquid water with columnar amounts around 100 g m^{-2} inside the anvil cloud. While most radar Doppler spectra within the mammatus lobes show a singular peak with typical ice/snowfall velocities of around 1 m s^{-1}, in the region of strong lidar attenuation we also find bimodal spectra with a second smaller peak close to 0 m s^{-1} hinting at supercooled droplets (Fig. 8). The supercooled droplet layer detected by the lidar also coincides with the largest vertical Z_e gradient (Fig. 6). The Doppler spectral width measurements in Fig. 7 also show virga (i.e., streaks of particles with enhanced spectral width falling out of the lidar-detected liquid layer) (e.g., between 1735 and 1737 UTC).

Similar to many other studies of combined radar–lidar observations of mixed-phase cloud systems (see, e.g., Hogan et al. 2003), the supercooled-liquid layer detected by the lidar is above the cloud boundaries derived from radar reflectivity. This is consistent with relatively large particles (i.e., effective radii $>25\,\mu$m) (Donovan and van Lammeren 2001), because sedimentation of aggregated or large single ice particles from the liquid layer results in a larger radar signal (with a D^6 dependence) relative to the lidar signal (with a D^2 dependence). Taking again the polarimetric C-band radar data into account, aggregation can be considered as less dominant and platelike crystal growth as more likely in this case study, since aggregation results in an increase of Z_H toward lower heights as opposed to the decrease

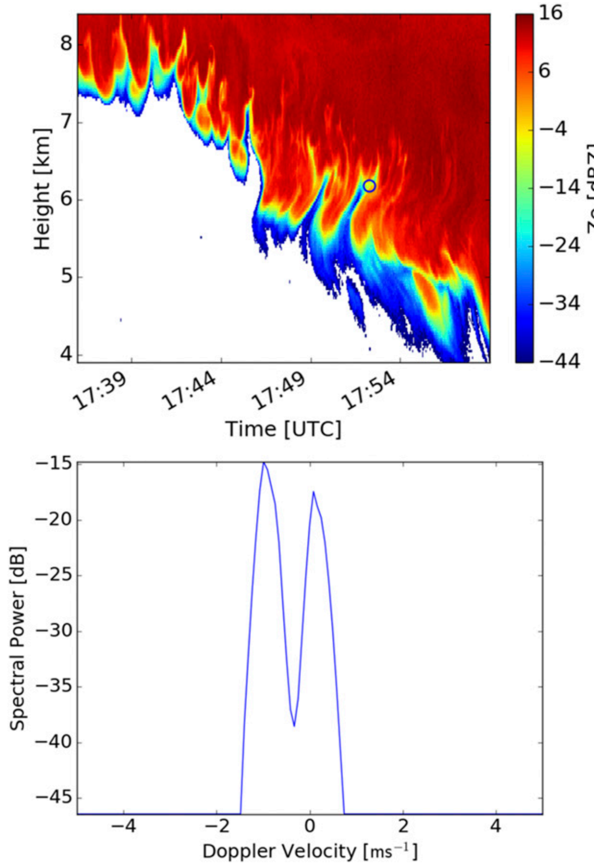

FIG. 8. (top) As in Fig. 6, a detailed zoom in the underside of the anvil with the most intense mammatus lobes showing the effective reflectivity factor measured with JOYRAD-35. (bottom) The blue dot in (top) indicates the location of the Doppler spectrum.

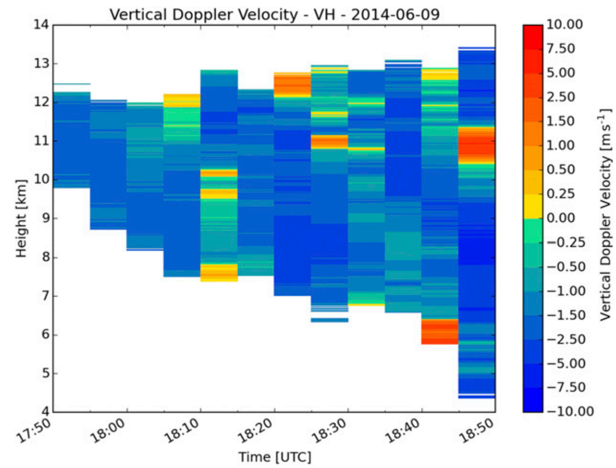

FIG. 9. Vertical Doppler velocity measured with the BoXPol birdbath scan. In the detected mammatus region updrafts up to 1 m s^{-1} and along the entire leading anvil updrafts between 0.5 and 2.5 m s^{-1} are detected. Note that the measurements are made every 5 min, thus, the display is not continuous in time.

observed. Studies of lidar observations in mixed-phase clouds consistently show large depolarization ratio values beneath supercooled layers, which are only consistent with nonspherical particles (e.g., Sassen 2005; Shupe 2007; Seifert et al. 2010; Bühl et al. 2016). Unfortunately, no polarimetric lidar information is yet available at JOYCE.

Close to the time of the C-band cross section displayed in Fig. 5, JOYRAD-35 shows localized areas of upward motion in the sloping anvil base. Doppler velocities reach 1.5 m s^{-1} (Fig. 6, middle panel) in accordance with the updrafts in mammatus lobes measured with the Doppler lidar (not shown). Also, the BoXPol birdbath scan (Fig. 9) over Bonn about 45 min later measured upward vertical velocities of 0.5–1.5 m s^{-1} in the mammatus region. Along the entire leading anvil, areas of upward motion up to 2.5 m s^{-1} are measured. According to Rauber and Tokay (1991), much weaker updrafts can already produce liquid water in reasonable amounts; they estimated that at −22°C upward motion of 0.03 m s^{-1} is sufficient. These drops must coexist with ice particles, although the amount of ice seems to be insufficient to deplete the generated liquid water drops. Revisiting Fig. 6, the velocities within the mammatus pouches vary between −1.5 and +1.5 m s^{-1} while relatively strong downdrafts of up to −5 m s^{-1} are observed 0.5–1 km above the base of the mammatus. Since no radiosonde information through the mammatus region is available, we cannot rule out whether the presence of a stable layer weakened the downdrafts at lower altitudes.

Kollias et al. (2005) interpret the collocation of layers of higher Doppler spectral width with Doppler velocity gradients in mammatus as an indication of high turbulence. Measured Doppler spectral widths at about 0.5–1 km above the radar-detected base of the pouches are around 0.8 m s^{-1} and reach up to 1.2 m s^{-1} (Fig. 6, bottom panel). Neglecting wind shear, the main contributions to the observed Doppler spectrum width are the variability in the terminal velocities of hydrometeors and the radar subresolution volume turbulence (Kollias et al. 2001). Using the mean spectral width above the mammatus region as an estimator for contribution of the difference in terminal velocities ($\sigma_d = 0.2$ m s^{-1}), spectral widths σ around 0.8 m s^{-1} at 8-km heights (Fig. 10) would, according to Fang et al. 2014 (we insert the estimated variance due to air turbulence $\sigma_t^2 = \sigma^2 - \sigma_d^2$ in their equation), correspond to 185 cm^2 s^{-3}, which would be consistent with the values estimated by Kollias et al. (2005) in mammatus. Such high turbulence is typically observed in shallow cumuli, whereas dissipation rates of high clouds are usually smaller (Kollias et al. 2001).

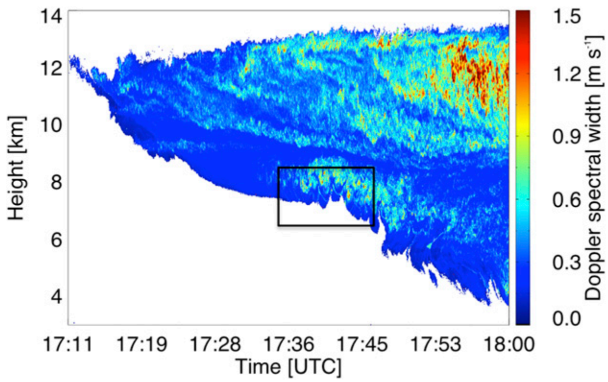

FIG. 10. Spectral width of a larger portion of the leading anvil measured by JOYRAD-35 on 9 Jun 2014. The black box indicates the time–height–space displayed as zoomed-in view of the most intense mammatus region in Fig. 6 [(bottom) with a different color bar in order to highlight the fall streaks].

The cloud radar Doppler spectral width for a larger area of the anvil (Fig. 10) shows another layer of increased spectral width/turbulence sloping down toward the storm center. Between 1715 and 1750 UTC, a layer with spectral width values around $0.8\,\mathrm{m\,s^{-1}}$ descends from 11.5 km down to 8.5 km in height. This layer is clearly separated from the shorter-lasting turbulent layer observed between 1730 and 1750 UTC much closer to the mammatus lobes. Martner (1995) and Kollias et al. (2005) also report descending layers of high turbulence near the cloud base prior to mammatus formation and argued that the origin of the mammatus bulges is deep in the anvil cloud. Interestingly, the Doppler velocity spectrum between both layers identified in the Pentecost case is positively skewed (cf. Figs. 10 and 11, top panel) with the mean Doppler velocity dominated by the downward-moving hydrometeors, which are probably ice crystals. But the spectra clearly suggest upward-moving particles at up to $2\,\mathrm{m\,s^{-1}}$ (Fig. 11, bottom panel). This updraft signature in the spectra and the skewness of the spectrum suggest increased depositional growth of ice particles in this layer.

Kollias et al. (2005) report the presence of gravity waves near a cirrus anvil base with mammatus. Our observations of the cloud radar Doppler velocity of the trailing anvil (Fig. 12) also indicate that at least parts of the Z_{DR} signals observed by the C-band radars are associated with gravity waves. Since the bow echo passed with a speed of about $85\,\mathrm{km\,h^{-1}}$, the wavelength can be roughly estimated to be around 7 km. We could not, however, identify clear signatures of gravity waves in the mammatus region of the leading anvil. Moreover, Fig. 12 shows long wavelength gravity waves in the Doppler velocity with alternating positive and negative velocities when no mammatus lobes can be identified. Also, the

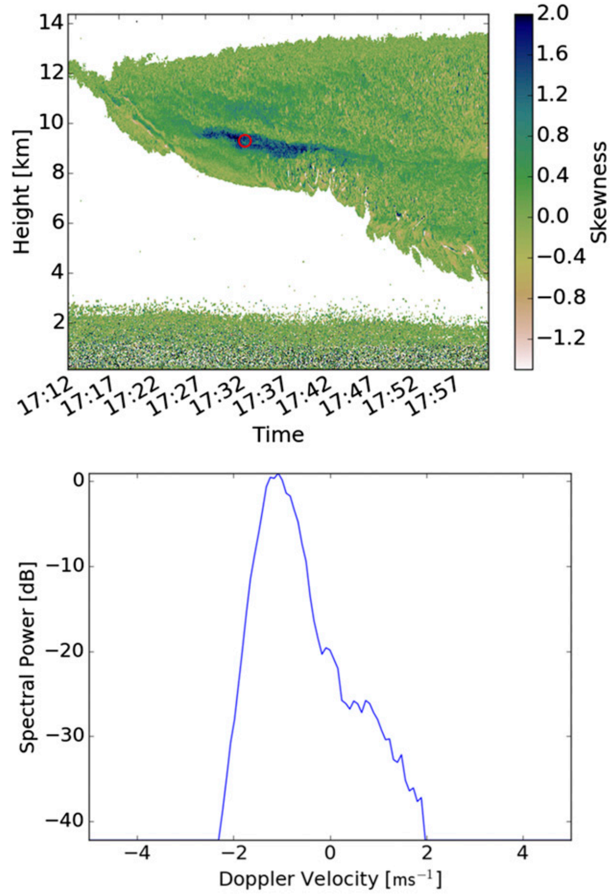

FIG. 11. (top) Skewness of the Doppler spectrum of a larger portion of the leading anvil measured by JOYRAD-35 on 9 Jun 2014. (bottom) The red circle in (top) indicates the location of the sample Doppler spectrum. Again, the convention of positive velocities for upward motion is used.

collocated 1.5-μm Doppler lidar measurements do not show a clear supercooled liquid layer in the trailing anvil. Since no additional cloud radar observations or TSI measurements (owing to the time being after sunset) of the trailing anvil are available, it remains unclear whether parts of the detected Z_{DR} signal in the trailing anvil are associated with mammatus and/or gravity waves.

6. Polarimetric radar observations of mammatus in Oklahoma

Signatures similar to the 2014 Pentecost storms have been observed in mammatus associated with supercells in Oklahoma. Figure 13 shows a reconstructed RHI of Z_H and Z_{DR} through a tornadic storm observed on 29 May 2004 by KOUN, an S-band WSR-88D in central Oklahoma. As in the observations from Germany, there are regions of enhanced Z_{DR} with peak values up to 2 dB

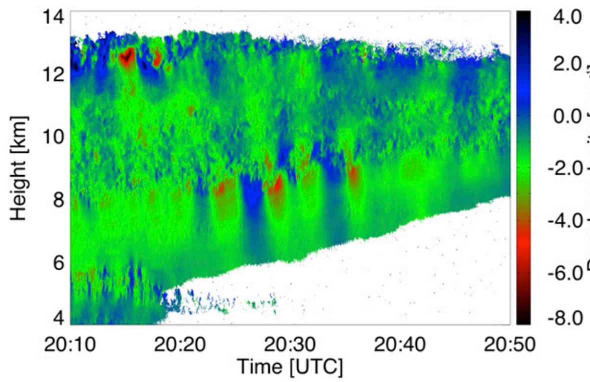

FIG. 12. Doppler velocity (positive values indicate upward motions) of a larger portion of the trailing anvil measured by JOYRAD-35 on 9 Jun 2014.

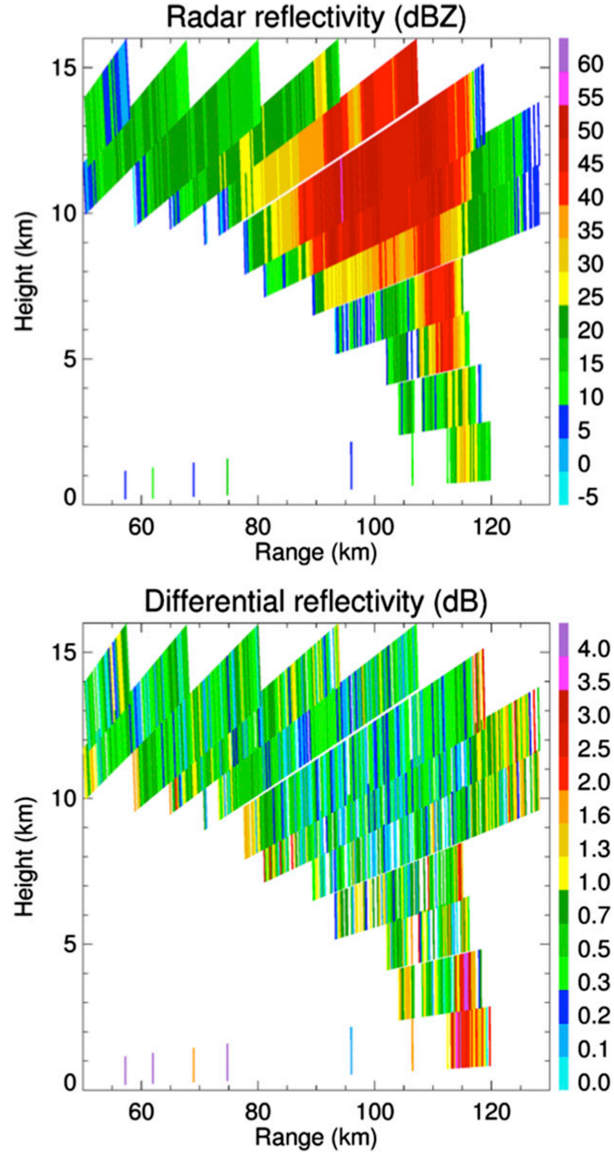

FIG. 13. Reconstructed range–height indicator (RHI) measured with the S-band radar in Oklahoma during a strong tornadic storm on 29 May 2004. The different panels show the polarimetric variables horizontal reflectivity Z_H and differential reflectivity Z_{DR}.

along the lower portion of the sloping cumulonimbus anvil associated with mammatus. Again, Z_H decreases and Z_{DR} rapidly increases toward the bottom of the anvil signaling differential sedimentation of liquid drops or other hydrometeors. Note that the Z_{DR} enhancement at the rear side of the storm at the distances exceeding 115 km and heights between 9 and 14 km is attributed to the effect of three-body scattering associated with an elevated hail core (Hubbert and Bringi 2000; Picca and Ryzhkov 2012).

Widespread mammatus were observed with severe thunderstorms that developed across portions of the south-central United States on the afternoon of 13 April 2014. Data from KTLX, a nearby polarimetric WSR-88D located in central Oklahoma, indicated enhanced Z_{DR} of 1–4 dB collocated with low Z_H (e.g., less than 15 dBZ) along the lower edge of an anvil associated with mammatus as seen in data from an 8.0° elevation angle scan (Fig. 14). The height where wet-bulb temperature is equal to 0°C was about 2.5 km for this case while the ambient environmental temperature at the storm anvil base varies between approximately −8° and −18°C. One can see from the right-bottom panel in Fig. 14 that the patches of Z_{DR} enhancement are detected only in certain areas of the anvil in these particular severe storms. Owing to a relatively low signal-to-noise ratio, the variance in the Z_{DR} estimates is likely to be higher in this area (near the base of the anvil) than in areas of the anvil where the return signal is stronger. As such, some caution is warranted when looking at the exact Z_{DR} maxima.

In general, having examined additional six mammatus events (not shown) associated with supercells observed by polarimetric WSR-88Ds in the central United States, lobes of enhanced Z_{DR} are often not observed in thunderstorm anvils [e.g., Homeyer and Kumjian (2015) did not find such signatures in anvils of their convective storm composites]. This is especially true for the cases with high signal-to-noise ratio where one can have greater confidence in the Z_{DR} maxima. We suspect there are at least two possible reasons for this: 1) the microphysical processes associated with these regions of enhanced Z_{DR} in mammatus are not always present, and 2) the characteristic size of mammatus are often too small relative to the radar resolution volume (i.e., the radar cannot spatially resolve the mammatus lobes and associated Z_{DR} signatures). Better sampling of mammatus

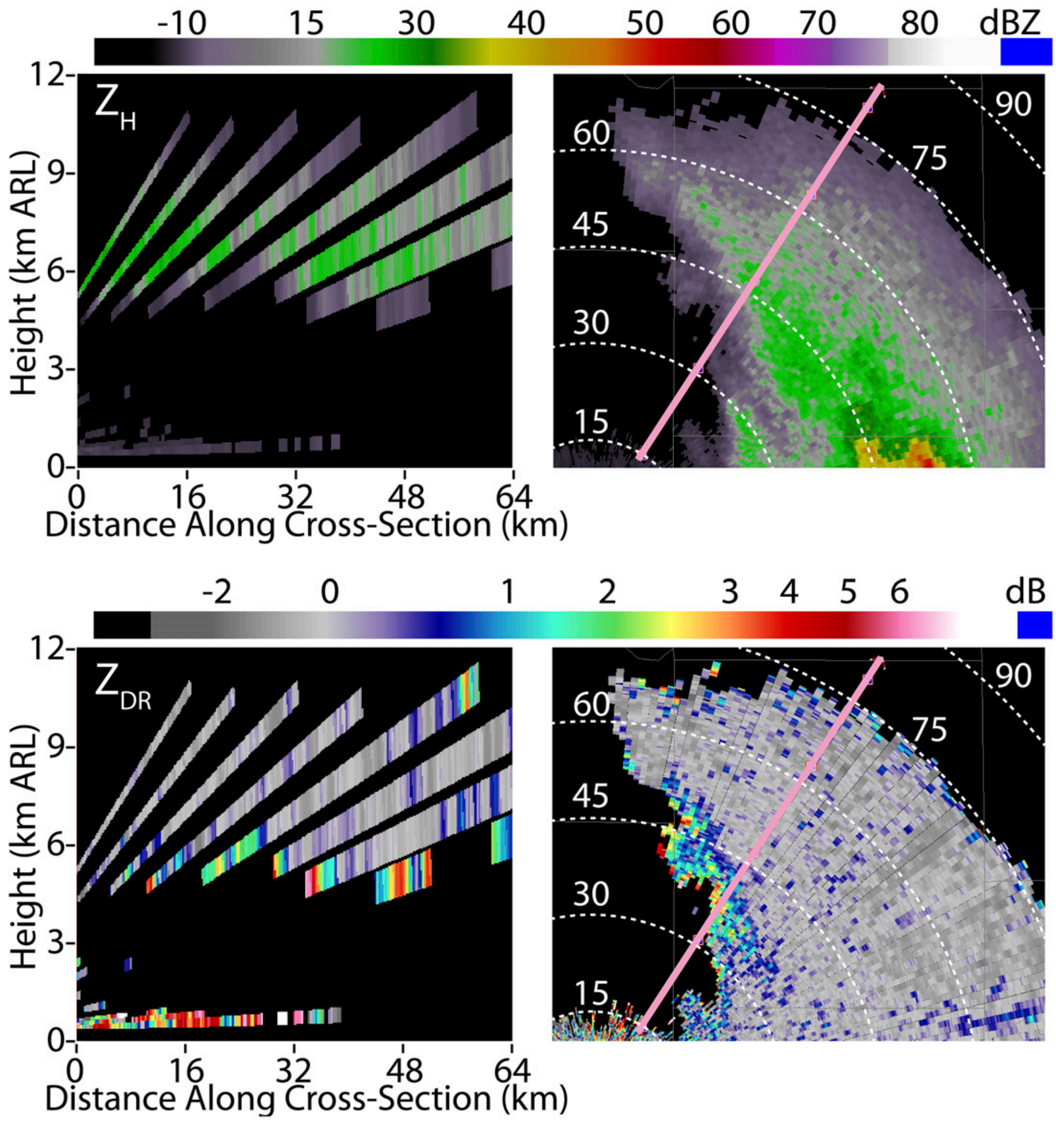

FIG. 14. Plots of Z_H and Z_{DR} in vertical cross section (left) through the mammatus lobes and (right) at fixed antenna elevation 8.0° for the storm observed in central Oklahoma by the KTLX WSR-88D at 2231 UTC 13 Apr 2014. (right) White dashed lines indicate the distance from the radar. (left) Vertical cross section is displayed along the direction marked by a pink line in the right panels. Heights are labeled in units of km above radar level (ARL).

can be obtained by using nontraditional sampling strategies that include the collection of genuine RHIs, which can greatly increase the vertical resolution and data coverage when compared to traditional volume coverage patterns using the WSR-88D network.

Since the thunderstorm anvils may spread over large areas and are quite uniform horizontally, we utilize the recently introduced quasi-vertical profiles (QVP) methodology (Ryzhkov et al. 2016) to capture large-scale polarimetric features of the anvil of a supercell storm observed with the KTLX WSR-88D on 19 May 2013 (Fig. 15). The QVP technique uses azimuthal averaging of the radar data collected at high antenna elevation and presents the resulting quasi-vertical profiles of Z_H, Z_{DR}, ρ_{hv}, and K_{DP} in a height versus time format as shown in Fig. 15. To generate the QVP for K_{DP}, K_{DP} is computed first for each radial and then azimuthally averaged. The antenna elevation of 19.5° was used to generate QVPs for this case so that the diameter of the circle over which data are averaged varies from 27.5 to 55 km for the height changing from 5 to 10 km. Such an average profile is not adequate to reveal important microphysical features of the most intense convective part of the storm as it passed over the radar

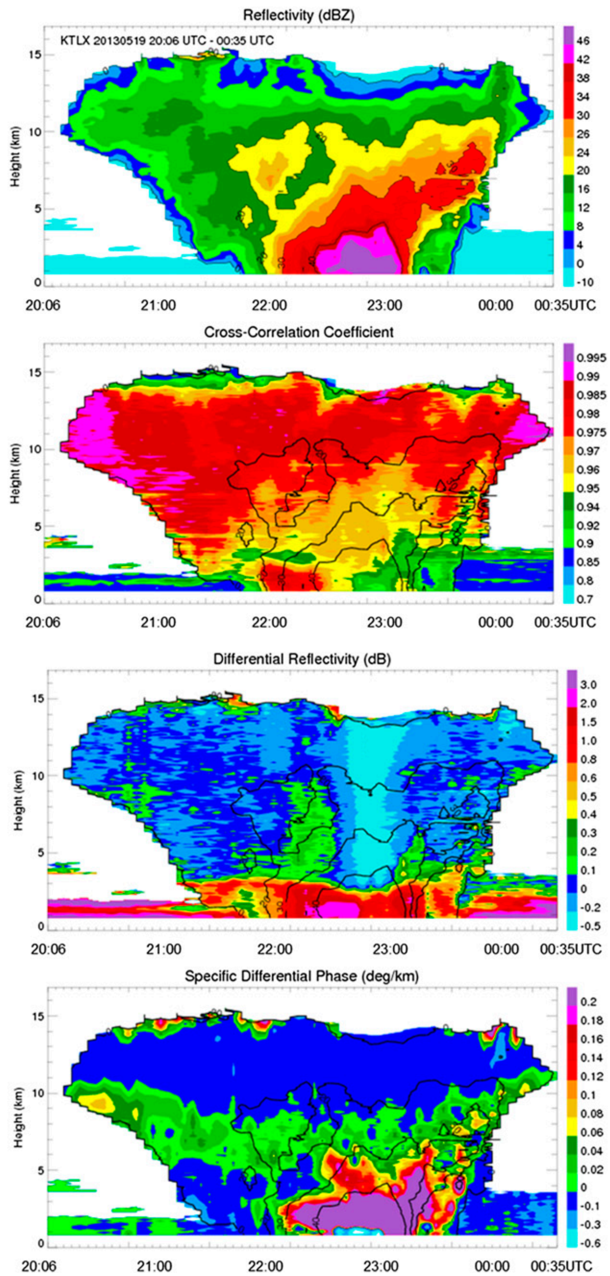

FIG. 15. QVPs of Z_H, Z_{DR}, ρ_{hv}, and K_{DP} generated from the data collected at elevation 19.5° by the KTLX WSR-88D for the supercell storm in Oklahoma on 19 May 2013.

between 2200 and 2300 UTC, but it is satisfactory to identify interesting polarimetric signatures in its anvil (time before 2130 UTC). Most notable of them is the K_{DP} enhancement in the lower part of the anvil. The value of K_{DP} estimate is usually quite low and noisy in the ice portions of the storms at S band, but the azimuthal averaging helps to significantly reduce the statistical errors and make it possible to roughly quantify ice water content (IWC) using the following relation:

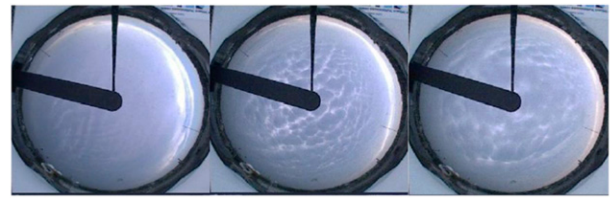

FIG. 16. Snapshots taken with the total sky imager located at the JOYCE site (left) 1730, (middle) 1740, and (right) 1750 UTC indicating roughly the time period with clearly visible mammatus lobes.

$$\mathrm{IWC} = 3.2K_{\mathrm{DP}} \tag{1}$$

from Vivekanandan et al. (1994) and Ryzhkov et al. (1998). [In (1), IWC is expressed in grams per cubic meter and K_{DP} in degrees per kilometer.] Figure 15 shows that K_{DP} near the base of the anvil varies between 0.04° and 0.08° km^{-1}, which corresponds to IWC within the 0.13–0.26 g m^{-3} range according to (1). Because of the similarity with the signature of dendritic growth often observed in the temperature range of around −15°C (e.g., Kennedy and Rutledge 2011; Bechini et al. 2013), the enhancement of K_{DP} in the lower part of anvil shifted downward from the local Z_H maximum testifies for depositional growth of anisotropic ice there (see section 7c for a more detailed discussion of the signature).

7. Characterization of anvil mammatus

a. *Spatial and temporal scales*

The German C-band radar composite allowed for the continuous monitoring of the Z_{DR} signatures of anvil mammatus of the supercell storm crossing northern Germany from the west toward the northeast for a period of more than 6 hours. We conclude from the observations in Germany and the United States that only a small fraction of mammatus exhibits the Z_{DR} signatures. Schultz et al. (2006) conclude from earlier observations that the lifetime of a mammatus field can range from 15 min to a few hours. The Pentecost mammatus fields indicated by the Z_{DR} signals in the C-band composite (Figs. 4 and 5) roughly covered 30 km in the west–east direction and more than 100 km in the north–south direction. The time period mammatus were observed by the TSI (Fig. 16) support such extended fields and durations. Mammatus or upward motion associated with gravity waves (or a mixture of both) as detected in the Z_{DR} column product in the trailing anvil of the bow echo and after its passage (Fig. 3) occupied a smaller area; also the magnitudes of the Z_{DR} column product were smaller. Individual mammatus lobes had diameters between 1 and 3 km in the horizontal and up to 1 km in the vertical (Fig. 2) in accordance with magnitudes given by Schultz et al. (2006). Horizontal scales below 1 km (Clarke 1962; Warner 1973) and up to 7 km (Wang and Sassen 2006), however, have also been observed.

b. Microphysics

During the Pentecost event, mammatus were observed between 6- and 8-km height where temperatures were between −15° to −28°C. The maximum vertical motions in the mammatus region (Figs. 7 and 11) are between 0.5 and 1.5 m s^{-1} and promote the existence of supercooled liquid in these anvil mammatus. This interpretation is corroborated by cloud radar, Doppler lidar (Fig. 7), and microwave radiometer observations.

Both the cloud radar and C-band signatures suggest circulations within mammatus lobes similar to what was probably first documented by Winstead et al. (2001) in a cumulonimbus anvil mammatus and also observed by Kollias et al. (2005) in mammatus in a deep cirrus layer. Figure 6 shows (most clearly within the intense lobes between 1735 and 1740 UTC) downward vertical velocities of up to 4 m s^{-1} in the center of the mammatus lobes and upward motion of up to 1.5 m s^{-1} along the edges in agreement with the two referred studies. When comparing Doppler velocity and effective reflectivity estimated by the cloud radar (Fig. 6), the intense lobe centers coincide with descending motion and higher reflectivity than in between. Martner (1995, 1996) and others also reported negative correlations between Doppler velocity and reflectivity visible in Fig. 6. Schultz et al. (2006) reasoned that because of the higher reflectivities the downward-protruding lobes should also contain the larger hydrometeors. While supercooled liquid droplets at very low subfreezing temperatures between the lobes are clearly documented in our observations, their expected sizes are insufficient to explain the high observed Z_{DR} values in and around mammatus.

c. Indications for highly anisotropic ice crystals

Based on the pronounced polarimetric signature observed at the underside of the mammatus bearing anvils, we suggest that highly anisoptropic ice crystals are perhaps the dominant hydrometeor type at the base of the mammatus. In most ice clouds, pristine crystals are generated near the top of the clouds, which grow during the fall by deposition, aggregation, or riming. According to Kennedy and Rutledge (2011) the signature of dendritic growth especially consists of a band of high K_{DP} in an area of low ρ_{HV} and relatively low Z_H near the −15°C environmental temperature level. Dendritic growth, however, has also been found to produce a band of enhanced Z_{DR} (Andrić et al. 2013). Both aggregation and riming tend to reduce Z_{DR} due to the decrease of bulk density and/or oblateness. Hence, Z_H increases, Z_{DR} decreases, and ρ_{HV} increases with decreasing height (i.e., toward the ground) where riming and aggregation occur. In our observations, we see the same polarimetric signature as expected with dendritic growth: higher Z_{DR} together with lower Z_H and lower ρ_{HV}. Andrić et al. (2013) and Kennedy and Rutledge (2011) associated bands of high Z_{DR} and high K_{DP} as a tell-tale sign of dendritic growth, but the Z_{DR} and K_{DP} bands do not necessarily occur together. For example, Bechini et al. (2013) noted a vertical offset between these bands when they occur at the same time, and Moisseev et al. (2015) argue for different physical processes responsible for Z_{DR} and K_{DP} bands; they associate high K_{DP} with dendritic growth under high number concentrations promoting the onset of aggregation, while bands of high Z_{DR} in an absence of enhanced K_{DP} indicate dendritic growth under low number concentrations.

Applying these findings to the Pentecost anvil mammatus, the observed higher Z_{DR}, lower Z_H, lower ρ_{HV}, and vertically nearly constant K_{DP} seem to indicate that depositional growth and maybe also new nucleation of particles occurs in the highly supersaturated anvil base region. The observed temperature range (−15° to −30°C) might include dendrites but in general can only be associated to preferentially platelike particles (e.g., Bailey and Hallett 2009). Seeding from ice particles falling from higher levels in the supersaturated region is a likely process in the anvil, but also glaciation of supercooled liquid cloud droplets generated in the localized updrafts is possible. The multisensor observations favor freezing nucleation over deposition nucleation due to the identified supercooled liquid layer (Vali et al. 2015). A more precise distinction between immersion freezing, contact freezing, and condensation freezing, however, is not possible. At higher altitudes where ascent intensity decreases (or where upward vertical motion is absent), the air is likely to be only supersaturated with respect to ice, hence liquid droplets may evaporate and/or ice crystals may grow at their expense according to the Bergeron–Findeisen mechanism. Comparing the Pentecost storm in Germany with the observations for the supercell storm in Oklahoma on 19 May 2013 (Fig. 15), the more pronounced K_{DP} signal in Fig. 15 hints toward higher concentration of platelike crystals in the Oklahoma case and smaller concentrations during the Pentecost storm. Note that simulations performed by Schrom et al. (2015) corroborate a greater variability of Z_{DR} with the maximum dimension of plates compared to dendrites. Both dendrites and plates become more oblate with increasing size but the growing branches of the dendrites also results in a decrease of the density, which counteracts the increase in aspect ratio (Botta et al. 2013; Lu et al. 2014).

These conclusions are generally in agreement with findings from several others (e.g., Sassen 2005; Shupe 2007; Westbrook et al. 2010; Seifert et al. 2010; Buehl et al. 2016). Their synergistic Doppler lidar and polarimetric cloud radar observations or depolarization lidar observations show consistently large depolarization ratios below supercooled layers, which led them to conclude that oriented planar ice crystals are frequently falling from supercooled liquid layers. These studies indicate that pristine crystals nucleate locally or seeding from higher levels occurs and, subsequently, the crystals grow rapidly within the supercooled layer before falling out.

8. Summary and outlook

The analysis of the distribution of pseudo-Z_{DR} columns during the Pentecost 2014 event in North Rhine-Westfalia, Germany, revealed unexpected potential updraft zones in the leading and trailing anvil tens of kilometers away from the core of intense convective storms. These Z_{DR} signals were generated by fundamentally different processes than those associated with Z_{DR} columns. The latter have been observed near updrafts of convective storms (and nearer the main storm ''core'') and are indicative of incipient convective development or mature convective storms. When examining these data, it became clear that the Z_{DR} signatures far downstream of the majority of the Z_H in the Pentecost event were detached from the melting layer, which stood in contrast to the current understanding of Z_{DR} columns (which are thought to be composed of large raindrops that are in the process of freezing and wet hail); the observed polarimetric signals, instead, were associated with storm anvil mammatus.

These findings spurred intense investigations of other remote sensing observations of the storm by a polarimetric X-band radar, a vertically pointing Ka-band Doppler cloud radar, a Doppler lidar, a microwave radiometer, a ceilometer, and a total sky imager, which clearly identified regions of upward vertical velocity in the leading anvil associated with anvil mammatus. The Z_{DR} signals in the trailing anvil, however, could not be that clearly attributed to mammatus. The Ka-band cloud radar observations point to gravity waves but do not show the characteristic mammatus lobes. A much larger dataset needs to be analyzed, however, to demonstrate the applicability of a modified Z_{DR} column algorithm for automated storm anvil mammatus monitoring.

Along the sloping bases of the cumulonimbus anvil clouds associated with the mammatus, Z_H and ρ_{HV} decrease toward the bottom of the anvil while Z_{DR} rapidly increases, and similar signatures have also been observed in the anvils of supercell storms in the United States. These patterns are found in regions of the anvil with relatively strong updrafts (up to $1.5\,\mathrm{m\,s^{-1}}$) documented by other remote sensing instruments for the German case. These updrafts, which are located between the mammatus lobes, should be capable of generating supercooled liquid water that was also detected. About 0.5–1 km above the radar-detected base of the mammatus lobes, an area of enhanced turbulence was identified. Further evidence taken from other remote sensing observations below supercooled liquid layers in mixed-phase clouds let us conclude that the pronounced polarimetric signatures including the high Z_{DR} values at subfreezing temperatures in the mammatus are most probably associated with horizontally oriented anisotropic ice crystals that grow in the supercooled liquid layer near the bottom of the anvil.

Layers of increased Doppler spectral width and significant gradients in mean Doppler velocity slightly above the base of the mammatus are indicative of turbulence. At higher levels in the anvil, additional less turbulent layers can be identified. The association of anvil mammatus with supercooled liquid water renders mammatus detection also important for aviation safety. These zones appear far away from strong surface precipitation and might be missed by air traffic control systems. The turbulence, at least in the cases investigated, is not in a threatening range for aviation safety. The networks of operational dual-polarization radars similar to the one employed by the U.S. National Weather Service or DWD in Germany may offer a unique opportunity to detect such areas.

Besides their impressive sights, anvils associated with cumulonimbus clouds also play an important role in radiative transfer (e.g., Garrett et al. 2010; Houze 2014). Given the evidence of rather small-scale processes acting and shaping the anvil—like the mammatus—we may suspect that their representation in dynamic atmospheric models might be too simplistic. The observations and interpretations presented here supplemented by further studies should be considered in future efforts to improve these models.

This paper discusses only a few supercell cases and does not allow us to draw general conclusions about mammatus in supercells or in other clouds like cirrus, cirrocumulus, altocumulus, altostratus, stratocumulus, and volcanic ash clouds. The observed turbulent regions above the mammatus lobes and the supercooled liquid layer may be caused by the supercell environment and are thus not necessarily also characteristic of mammatus in other cloud types.

Acknowledgments. The research of Silke Trömel and Malte Diederich was partly carried out in the framework of the Hans-Ertel-Centre for Weather Research (http://www.herz-tb1.uni-bonn.de/). This research network of universities, research institutes, and the Deutscher Wetterdienst (DWD) is funded by the BMVBS (Federal Ministry of Transport, Building and Urban Development). Malte Diederich was also supported by the SFB TR32 (Transregional Collaborative Research Centre 32) funded by the DFG (German Research Foundation). Alexander Ryzhkov and Jeffrey Snyder were supported via funding from NOAA/University of Oklahoma Cooperative Agreement NA11OAR4320072 under the U.S. Department of Commerce and from the National Science Foundation (Grant AGS-1143948). Stefan Kneifel acknowledges funding by the Federal Ministry of Education and Research (BMBF) within the program High Definition Clouds and Precipitation for Advancing Climate Prediction [HD(CP)^2] under Grant HD(CP)^2 01LK1210C. We gratefully acknowledge the support by the Deutscher Wetterdienst for providing the C-band radar data for Germany and the support by the SFB TR32 for providing the BoXPol data. We also thank Max Maahn and Jan Schween (University of Cologne) for processing of the JOYRAD-35 data and helpful discussions about the Doppler lidar data. Finally, the authors acknowledge the Editor-in-Chief David M. Schultz and the reviewers for their careful and valuable input for improvements of the paper.

REFERENCES

Anagnostou, E. N., and W. F. Krajewski, 1999: Real-time radar rainfall estimation. Part 1: Algorithm formulation. *J. Atmos. Oceanic Technol.*, **16**, 189–197, doi:10.1175/1520-0426(1999)016<0189:RTRREP>2.0.CO;2.

Andrić, J., M. R. Kumjian, D. Zrnić, J. M. Straka, and V. M. Melnikov, 2013: Polarimetric signatures above the melting layer in winter storms: An observational and modeling study. *J. Appl. Meteor. Climatol.*, **52**, 682–700, doi:10.1175/JAMC-D-12-028.1.

Bailey, M. P., and J. Hallett, 2009: A comprehensive habit diagram for atmospheric ice crystals: Confirmation from the laboratory, AIRS II, and other field studies. *J. Atmos. Sci.*, **66**, 2888–2899, doi:10.1175/2009JAS2883.1.

Baldauf, M., A. Seifert, J. Förstner, D. Majewski, M. Raschendorfer, and T. Reinhardt, 2011: Operational convective-scale numerical weather prediction with the COSMO model: Description and sensitivities. *Mon. Wea. Rev.*, **139**, 3887–3905, doi:10.1175/MWR-D-10-05013.1.

Beatty, K., E. N. Rasmussen, and J. M. Straka, 2008: The supercell spectrum. Part I: A review of research related to supercell precipitation morphology. *Electron. J. Severe Storms Meteor.*, **3** (4). [Available online at http://www.ejssm.org/ojs/index.php/ejssm/article/viewarticle/44/45.]

Bechini, R., L. Baldini, and V. Chandrasekar, 2013: Polarimetric radar observations in the ice region of precipitating clouds at C-band and X-band radar frequencies. *J. Appl. Meteor. Climatol.*, **52**, 1147–1169, doi:10.1175/JAMC-D-12-055.1

Bellon, A., F. Fabry, and G. L. Austin, 1991: Errors due to space–time sampling strategies in high-resolution radar data in hydrology. Preprints, *25th Conf. on Radar Meteorology*, Paris, France, Amer. Meteor. Soc., 2040–2048.

Benjamin, S. G., and T. N. Carlson, 1986: Some effects of surface heating and topography on the regional severe storm environment. Part I: Three-dimensional simulations. *Mon. Wea. Rev.*, **114**, 307–329, doi:10.1175/1520-0493(1986)114<0307:SEOSHA>2.0.CO;2.

Bluestein, H. B., and C. R. Parks, 1983: A synoptic and photographic climatology of low precipitation severe thunderstorms in the southern plains. *Mon. Wea. Rev.*, **111**, 2034–2046, doi:10.1175/1520-0493(1983)111<2034:ASAPCO>2.0.CO;2.

Botta, G., K. Aydin, and J. Verlinde, 2013: Variability in millimeter wave scattering properties of dendritic ice crystals. *J. Quant. Spectrosc. Radiat. Transfer*, **131**, 105–114, doi:10.1016/j.jqsrt.2013.05.009.

Bringi, V. N., and V. Chandrasekar, 2001: *Polarimetric Doppler Weather Radar: Principles and Applications.* Cambridge University Press, 636 pp.

Bühl, J., P. Seifert, A. Myagkov, and A. Ansmann, 2016: Measuring ice- and liquid-water properties in mixed-phase cloud layers at the Leipzig Cloudnet station. *Atmos. Chem. Phys.*, **16**, 10 609–10 620, doi:10.5194/acp-16-10609-2016.

Chandrasekar, V., R. Keränen, S. Lim, and D. Moisseev, 2013: Recent advances in classification of observations from dual polarization weather radars. *Atmos. Res.*, **119**, 97–111, doi:10.1016/j.atmosres.2011.08.014.

Clarke, R. H., 1962: Pressure oscillations and fallout downdraughts. *Quart. J. Roy. Meteor. Soc.*, **88**, 459–469, doi:10.1002/qj.49708837808.

Clough, S. A., and R. A. A. Franks, 1991: The evaporation of frontal and other stratiform precipitation. *Quart. J. Roy. Meteor. Soc.*, **117**, 1057–1080, doi:10.1002/qj.49711750109.

Delanoë, J., and R. J. Hogan, 2010: Combined CloudSat-CALIPSO-MODIS retrievals of the properties of ice clouds. *J. Geophys. Res.*, **115**, D00H29, doi:10.1029/2009JD012346.

Diederich, M., A. Ryzhkov, C. Simmer, P. Zhang, and S. Trömel, 2015: Use of specific attenuation for rainfall measurement at X-band radar wavelengths. Part I: Radar calibration and partial beam blockage estimation. *J. Hydrometeor.*, **16**, 487–502, doi:10.1175/JHM-D-14-0066.1.

Doms, G., and U. Schättler, 2002: A description of the nonhydrostatic regional model LM. Part I: Dynamics and numerics. *COSMO Newsl.*, **2**, 225–235.

Donovan, D. P., and A. C. A. P. van Lammeren, 2001: Cloud effective particle size and water content profile retrievals using combined lidar and radar observations: 1. Theory and examples. *J. Geophys. Res.*, **106**, 27 425–27 448, doi:10.1029/2001JD900243.

Doviak, R. J., and D. S. Zrnić, 2006: *Doppler Radar and Weather Observations.* Dover, 562 pp.

Fang, M., B. A. Albrecht, V. P. Ghate, and P. Kollias, 2014: Turbulence in continental stratocumulus. Part II: Eddy dissipation rates and large-eddy coherent structures. *Bound.-Layer Meteor.*, **150**, 361–380, doi:10.1007/s10546-013-9872-4.

Garrett, T. J., C. T. Schmidt, S. Kihlgren, and C. Cornet, 2010: Mammatus clouds as a response to cloud-base radiative heating. *J. Atmos. Sci.*, **67**, 3891–3903, doi:10.1175/2010JAS3513.1.

Glickman, T., Ed., 2000: *Glossary of Meteorology*. 2nd ed. Amer. Meteor. Soc., 855 pp. [Available online at http://glossary.ametsoc.org/.]

Görsdorf, U., V. Lehmann, M. Bauer-Pfundstein, G. Peters, D. Vavriv, V. Vinogradov, and V. Volkov, 2015: A 35-GHz polarimetric Doppler radar for long-term observations of cloud parameters—Description of system and data processing. *J. Atmos. Oceanic Technol.*, **32**, 675–690, doi:10.1175/JTECH-D-14-00066.1.

Heese, B., H. Flentje, D. Althausen, A. Ansmann, and S. Frey, 2010: Ceilometer lidar comparison: Backscatter coefficient retrieval and signal-to-noise ratio determination. *Atmos. Meas. Tech.*, **3**, 1763–1770, doi:10.5194/amt-3-1763-2010.

Hlad, C. J., Jr., 1944: Stability-tendency and mammatocumulus clouds. *Bull. Amer. Meteor. Soc.*, **25**, 327–331.

Hobbs, P. V., and A. L. Rangno, 1985: Ice particle concentrations in clouds. *J. Atmos. Sci.*, **42**, 2523–2549, doi:10.1175/1520-0469(1985)042<2523:IPCIC>2.0.CO;2.

Hogan, R. J., P. N. Francis, H. Flentje, A. J. Illingworth, M. Quante, and J. Pelon, 2003: Characteristics of mixed-phase clouds. I: Lidar, radar and aircraft observations from CLARE'98. *Quart. J. Roy. Meteor. Soc.*, **129**, 2089–2116, doi:10.1256/rj.01.208.

——, M. D. Behera, E. J. O'Connor, and A. J. Illingworth, 2004: Estimate of the global distribution of stratiform supercooled liquid water clouds using the LITE lidar. *Geophys. Res. Lett.*, **31**, L05106, doi:10.1029/2003GL018977.

Homeyer, C. R., and M. R. Kumjian, 2015: Microphysical characteristics of overshooting convection from polarimetric radar observations. *J. Atmos. Sci.*, **72**, 870–891, doi:10.1175/JAS-D-13-0388.1.

Houze, R. A., 2014: *Cloud Dynamics*. 2nd ed. Academic Press, 496 pp.

Hubbert, J., and V. Bringi, 2000: The effects of three-body scattering on differential reflectivity signatures. *J. Atmos. Oceanic Technol.*, **17**, 51–61, doi:10.1175/1520-0426(2000)017<0051:TEOTBS>2.0.CO;2.

Illingworth, A. J., J. W. F. Goddard, and S. M. Cherry, 1987: Polarization radar studies of precipitation development in convective storms. *Quart. J. Roy. Meteor. Soc.*, **113**, 469–489, doi:10.1002/qj.49711347604.

Kennedy, P. C., and S. A. Rutledge, 2011: S-band dual-polarization radar observations of winter storms. *J. Appl. Meteor. Climatol.*, **50**, 844–858, doi:10.1175/2010JAMC2558.1.

Kollias, P., B. A. Albrecht, R. Lhermitte, and A. Savtchenko, 2001: Radar observations of updrafts, downdrafts, and turbulence in fair weather cumuli. *J. Atmos. Sci.*, **58**, 1750–1766, doi:10.1175/1520-0469(2001)058<1750:ROOUDA>2.0.CO;2.

——, I. Jo, and B. A. Albrecht, 2005: High-resolution observations of mammatus in tropical anvils. *Mon. Wea. Rev.*, **133**, 2105–2112, doi:10.1175/MWR2918.1.

Kumjian, M. R., 2013: Principles and applications of dual-polarization weather radar. Part 1: Description of the polarimetric radar variables. *J. Oper. Meteor.*, **1**, 226–242, doi:10.15191/nwajom.2013.0119.

——, A. P. Khain, N. Benmoshe, E. Ilotoviz, A. V. Ryzhkov, and Vaughan T. J. Phillips, 2014: The anatomy and physics of Z_{DR} columns: Investigating a polarimetric radar signature with a spectral bin microphysical model. *J. Appl. Meteor. Climatol.*, **53**, 1820–1843, doi:10.1175/JAMC-D-13-0354.1.

Lewis, M. W., and S. L. Gray, 2010: Categorisation of synoptic environments associated with mesoscale convective systems over the UK. *Atmos. Res.*, **97**, 194–213, doi:10.1016/j.atmosres.2010.04.001.

Löhnert, U., and Coauthors, 2015: JOYCE: Jülich Observatory for Cloud Evolution. *Bull. Amer. Meteor. Soc.*, **96**, 1157–1174, doi:10.1175/BAMS-D-14-00105.1.

Long, C. N., J. M. Sabburg, J. Calbó, and D. Pagès, 2006: Retrieving cloud characteristics from ground-based daytime color all-sky images. *J. Atmos. Oceanic Technol.*, **23**, 633–652, doi:10.1175/JTECH1875.1.

Lu, Y., E. E. Clothiaux, K. Aydin, and J. Verlinde, 2014: Estimating ice particle scattering properties using a modified Rayleigh–Gans approximation. *J. Geophys. Res. Atmos.*, **119**, 10 471–10 484, doi:10.1002/2014JD021850.

Martner, B. E., 1995: Doppler radar observations of mammatus. *Mon. Wea. Rev.*, **123**, 3115–3121, doi:10.1175/1520-0493(1995)123<3115:DROOM>2.0.CO;2.

——, 1996: An intimate look at clouds. *Weatherwise*, **49**, 20–23, doi:10.1080/00431672.1996.9925404.

Moisseev, D. N., S. Lautaportti, J. Tyynela, and S. Lim, 2015: Dual-polarization radar signatures in snowstorms: Role of snowflake aggregation. *J. Geophys. Res. Atmos.*, **120**, 12 644–12 655, doi:10.1002/2015JD023884.

Moller, A. R., C. A. Doswell III, and R. W. Przybylinski, 1990: High-precipitation supercells: A conceptual model and documentation. Preprints, *16th Conf. on Severe Local Storms*, Kananaskis Park, Alberta, Canada, Amer. Meteor. Soc., 52–57.

——, M. P. Foster, and G. R. Woodall, 1994: The operational recognition of supercell thunderstorm environments and storm structures. *Wea. Forecasting*, **9**, 327–347, doi:10.1175/1520-0434(1994)009<0327:TOROST>2.0.CO;2.

North, G. R., J. Pyle, and F. Zhang, 2014: *Encyclopedia of Atmospheric Sciences.* 2nd ed. Academic Press, 2998 pp.

Oue, M., M. R. Kumjian, Y. Lu, Z. Jiang, E. E. Clothiaux, J. Verlinde, and K. Aydin, 2015: X-band polarimetric and Ka-band Doppler spectral radar observations of a graupel-producing Arctic mixed-phase cloud. *J. Appl. Meteor. Climatol.*, **54**, 1335–1351, doi:10.1175/JAMC-D-14-0315.1.

——, M. Galletti, J. Verlinde, A. Ryzhkov, and Y. Lu, 2016: Use of X-band differential reflectivity measurements to study shallow arctic mixed-phase clouds. *J. Appl. Meteor. Climatol.*, **55**, 403–424, doi:10.1175/JAMC-D-15-0168.1.

Pearson, G., F. Davies, and C. Collier, 2009: An analysis of the performance of the UFAM pulsed Doppler Lidar for observing the boundary layer. *J. Atmos. Oceanic Technol.*, **26**, 240–250, doi:10.1175/2008JTECHA1128.1.

Picca, J. C., and A. V. Ryzhkov, 2010: Z_{DR} columns as a predictive tool for hail growth and storm evolution. *25th Conf. on Severe Local Storms*, Denver, CO, Amer. Meteor. Soc., 11.3. [Available online at https://ams.confex.com/ams/25SLS/techprogram/paper_175750.htm.]

Picca, J., and A. Ryzhkov, 2012: A dual-wavelength polarimetric analysis of the 16 May 2010 Oklahoma City extreme hailstorm. *Mon. Wea. Rev.*, **140**, 1385–1403, doi:10.1175/MWR-D-11-00112.1.

Platt, C. M. R., R. T. Austin, S. A. Young, and A. J. Heymsfield, 2002: LIRAD observations of tropical cirrus clouds in MCTEX. Part II: Optical properties and base cooling in dissipating storm anvil clouds. *J. Atmos. Sci.*, **59**, 3163–3177, doi:10.1175/1520-0469(2002)059<3163:LOOTCC>2.0.CO;2.

Pruppacher, H. R., and J. D. Klett, 1996: *Microphysics of Clouds and Precipitation.* 2nd ed. Springer, 954 pp.

Rauber, R. M., and L. O. Grant, 1986: The characteristics and distribution of cloud water over the mountains of northern

Colorado during wintertime storms. Part II: Spatial distribution and microphysical characteristics. *J. Climate Appl. Meteor.*, **25**, 489–504, doi:10.1175/1520-0450(1986)025<0489:TCADOC>2.0.CO;2.

——, and A. Tokay, 1991: An explanation for the existence of supercooled water at the top of cold clouds. *J. Atmos. Sci.*, **48**, 1005–1023, doi:10.1175/1520-0469(1991)048<1005:AEFTEO>2.0.CO;2.

Ryzhkov, A., D. Zrnić, and B. Gordon, 1998: Polarimetric method for ice water content determination. *J. Appl. Meteor.*, **37**, 125–134, doi:10.1175/1520-0450(1998)037<0125:PMFIWC>2.0.CO;2.

——, P. Zhang, H. Reeves, M. Kumjian, T. Tschallener, S. Trömel, and C. Simmer, 2016: Quasi-vertical profiles—A new way to look at polarimetric radar data. *J. Atmos. Oceanic Technol.*, **33**, 551–562, doi:10.1175/JTECH-D-15-0020.1.

Sassen, K., 2005: Polarization in lidar. *Lidar: Range-Resolved Optical Remote-Sensing of the Atmosphere*, K. Weitkamp, Ed., Springer Series in Optical Sciences, Vol. 109, Springer, 19–42.

Schaefer, J. T., 1986: Severe thunderstorm forecasting: A historical perspective. *Wea. Forecasting*, **1**, 164–189, doi:10.1175/1520-0434(1986)001<0164:STFAHP>2.0.CO;2.

Schrom, R. S., M. R. Kumjian, and Y. Lu, 2015: Polarimetric radar signatures of dendritic growth zones within Colorado winter storms. *J. Appl. Meteor. Climatol.*, **54**, 2365–2388, doi:10.1175/JAMC-D-15-0004.1.

Schultz, D. M., and Y. Hancock, 2016: Contrail lobes or mamma? The importance of correct terminology. *Weather*, **71**, 203–209, doi:10.1002/wea.2765.

——, and Coauthors, 2006: The mysteries of mammatus clouds: Observations and formation mechanisms. *J. Atmos. Sci.*, **63**, 2409–2435, doi:10.1175/JAS3758.1.

Seifert, P., and Coauthors, 2010: Saharan dust and heterogeneous ice formation: Eleven years of cloud observations at a central European EARLINET site. *J. Geophys. Res.*, **115**, D20201, doi:10.1029/2009JD013222.

Shupe, M., 2007: A ground-based multiple remote-sensor cloud phase classifier. *Geophys. Res. Lett.*, **34**, L22809, doi:10.1029/2007GL031008.

Simmer, C., and Coauthors, 2015: Monitoring and modeling the terrestrial system from pores to catchments: The Transregional Collaborative Research Center on patterns in the soil–vegetation–atmosphere system. *Bull. Amer. Meteor. Soc.*, **96**, 1765–1787, doi:10.1175/BAMS-D-13-00134.1.

——, and Coauthors, 2016: HErZ: The German Hans-Ertel Centre for Weather Research. *Bull. Amer. Meteor. Soc.*, **97**, 1057–1068, doi:10.1175/BAMS-D-13-00227.1.

Snyder, J. C., A. Ryzhkov, M. Kumjian, J. Picca, and A. Khain, 2015: Developing a Z_{DR} column detection algorithm to examine convective storm updrafts. *Wea. Forecasting*, **30**, 1819–1844, doi:10.1175/WAF-D-15-0068.1.

Stith, J. L., 1995: In situ measurements and observations of cumulonimbus mamma. *Mon. Wea. Rev.*, **123**, 907–914, doi:10.1175/1520-0493(1995)123<0907:ISMAOO>2.0.CO;2.

Vali, G., P. J. DeMott, O. Möhler, and T. F. Whale, 2015: Technical note: A proposal for ice nucleation terminology. *Atmos. Chem. Phys.*, **15**, 10 263–10 270, doi:10.5194/acp-15-10263-2015.

van Delden, A., 1998: The synoptic setting of a thundery low and associated prefrontal squall line in western Europe. *Meteor. Atmos. Phys.*, **65**, 113–131, doi:10.1007/BF01030272.

Vivekanandan, J., V. Bringi, M. Hagen, and P. Meischner, 1994: Polarimetric radar studies of atmospheric ice particles. *IEEE Trans. Geosci. Remote Sens.*, **32**, 1–10, doi:10.1109/36.285183.

Wang, L., and K. Sassen, 2006: Cirrus mammatus properties derived from an extended remote sensing dataset. *J. Atmos. Sci.*, **63**, 712–725, doi:10.1175/JAS3648.1.

Warner, C., 1973: Measurements of mamma. *Weather*, **28**, 394–397, doi:10.1002/j.1477-8696.1973.tb00843.x.

Weissmann, M., and Coauthors, 2014: Initial phase of the Hans-Ertel Centre for Weather Research—A virtual centre at the interface of basic and applied weather and climate research. *Meteor. Z.*, **23**, 193–208, doi:10.1127/0941-2948/2014/0558.

Weitkamp, C., 2005: *Lidar: Range-Resolved Optical Remote Sensing of the Atmosphere.* Springer Series in Optical Sciences, Vol. 102, Springer, 460 pp.

Westbrook, C. D., A. J. Illingworth, E. J. O'Connor, and R. J. Hogan, 2010: Doppler lidar measurements of oriented planar ice crystals falling from supercooled and glaciated layer clouds. *Quart. J. Roy. Meteor. Soc.*, **136**, 260–276, doi:10.1002/qj.528.

Winstead, N. S., J. Verlinde, S. T. Arthur, F. Jaskiewicz, M. Jensen, N. Miles, and D. Nicosia, 2001: High-resolution airborne radar observations of mammatus. *Mon. Wea. Rev.*, **129**, 159–166, doi:10.1175/1520-0493(2001)129<0159:HRAROO>2.0.CO;2.

World Meteorological Organization, 1975: *International Cloud Atlas, Volume I: Manual on the Observation of Clouds and Other Meteors.* World Meteorological Organization Rep. WMO-407, 155 pp. [Available online at library.wmo.int/opac/index.php?lvl=notice_display&id=5357.]

——, 1987: *International Cloud Atlas, Volume II.* World Meteorological Organization Rep. WMO-407, 212 pp. [Available online at library.wmo.int/opac/index.php?lvl=notice_display&id=5358.]

Zrnić, D. S., and A. V. Ryzhkov, 1999: Polarimetry for weather surveillance radars. *Bull. Amer. Meteor. Soc.*, **80**, 389–406, doi:10.1175/1520-0477(1999)080<0389:PFWSR>2.0.CO;2.